JACS
JOURNAL OF THE AMERICAN CHEMICAL SOCIETY
Article
pubs.acs.org/JACS

Noncrystalline-to-Crystalline Transformations in Pt Nanoparticles

Long Li,[†,¶] Lin-Lin Wang,[‡] Duane D. Johnson,[‡,§] Zhongfan Zhang,[∥] Sergio I. Sanchez,[⊥] Joo H. Kang,[⊥] Ralph G. Nuzzo,[⊥] Qi Wang,[#] Anatoly I. Frenkel,[#] Jie Li,[▽] James Ciston,[○,◆] Eric A. Stach,[○] and Judith C. Yang*[,†]

[†]Chemical and Petroleum Engineering, and Physics, University of Pittsburgh, Pittsburgh, Pennsylvania 15261, United States
[‡]The Ames Laboratory (U.S. Department of Energy), Ames, Iowa 50011, United States
[§]Materials Science and Engineering, and Chemical and Biological Engineering, Iowa State University, Ames, Iowa 50011, United States
[∥]Mechanical Engineering and Materials Science, University of Pittsburgh, Pittsburgh, Pennsylvania 15261, United States
[⊥]Materials Research Laboratory, and Chemistry, University of Illinois at Urbana−Champaign, Urbana, Illinois 61801, United States
[#]Physics, Yeshiva University, New York, New York 10016, United States
[▽]Center for Research on Heath Care Data Center, University of Pittsburgh, Pittsburgh, Pennsylvania 15213, United States
[○]Center for Functional Nanomaterials, Brookhaven National Laboratory, Upton, New York 11973, United States
[◆]National Center for Electron Microscopy, Lawrence Berkeley National Laboratory, Berkeley, California 94720, United States

Supporting Information

ABSTRACT: We show that the noncrystalline-to-crystalline transition of supported Pt nanoparticles (NPs) in the subnanometer to nanometer size range is statistical in nature, and strongly affected by particle size, support, and adsorbates (here we use H_2). Unlike in the bulk, a noncrystalline phase exists and is stable in small NPs, reflecting a general mesoscopic feature. Observations of >3000 particles by high-resolution transmission electron microscopy show a noncrystalline-to-crystalline transition zone that is nonabrupt; there is a size regime where disordered and ordered NPs coexist. The NP size at which this transition occurs is strongly dependent on both the adsorbate and the support, and this effect is general for late 5d transition metals. All results are reconciled via a statistical description of particle-support-adsorbate interactions.

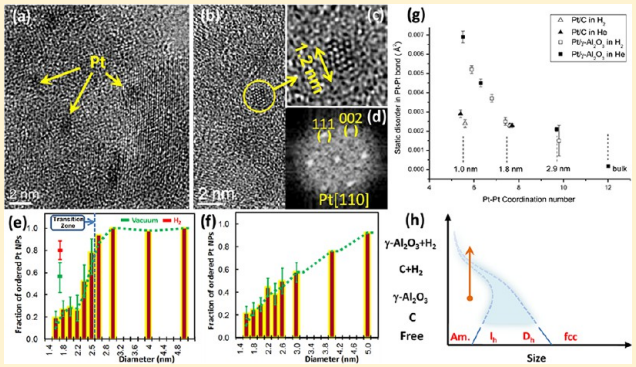

1. INTRODUCTION

The synthesis and unusual size-dependent properties of nanostructures between 1 and 10 nm (i.e., mesoscopic size ranges) are the subject of intense research due to their exceptional promise in advancing critical biomedical, chemical, electronic, and magneto/optical technologies. Metal nanoparticles (NPs) in this size range have many of their technologically interesting structure−property relationships bridge from atomic to bulklike behaviors, impacting a myriad of applications such as catalysis, drug delivery, magnetic devices, photonics, spintronics, and thermal/electrical transport.[1−5] In most applications, metal NPs are supported and used in a specific operational environment. Heterogeneous catalysis, which impacts the worldwide economy and sustainability due to its ubiquitous role in energy production, is but one example of a crucial area that depends sensitively on the three-dimensional structural habits of NPs, as well as their physicochemical structural sensitivity to the environment.[6−16] However, though fundamental descriptions of bulk and atomic properties of matter are well established, many basic but critical questions still remain unanswered in the mesoscopic regime. Does a material become mesoscopic, exhibiting neither bulklike nor molecular behavior, with a few atoms or hundreds of atoms? Is the bulk-to-cluster transition abrupt or is there a transition zone populated by mesoscopic systems with multiple energy barriers and metastable states? What is the appropriate language to describe mesoscopic materials and their size-dependent physicochemical behaviors? To address the above questions requires characterization of structure, chemical state, and phase transformations in real time and in their operational environments in order to detail mechanisms and kinetics.

Motivated by this need, improvements in nanocharacterization tools have rapidly accelerated, including extended X-ray absorption fine structure spectroscopy (EXAFS), X-ray photoelectron spectroscopy (XPS), X-ray diffraction (XRD), trans-

Received: June 1, 2013
Published: July 19, 2013

   dx.doi.org/10.1021/ja405497p | J. Am. Chem. Soc. 2013, 135, 13062−13072

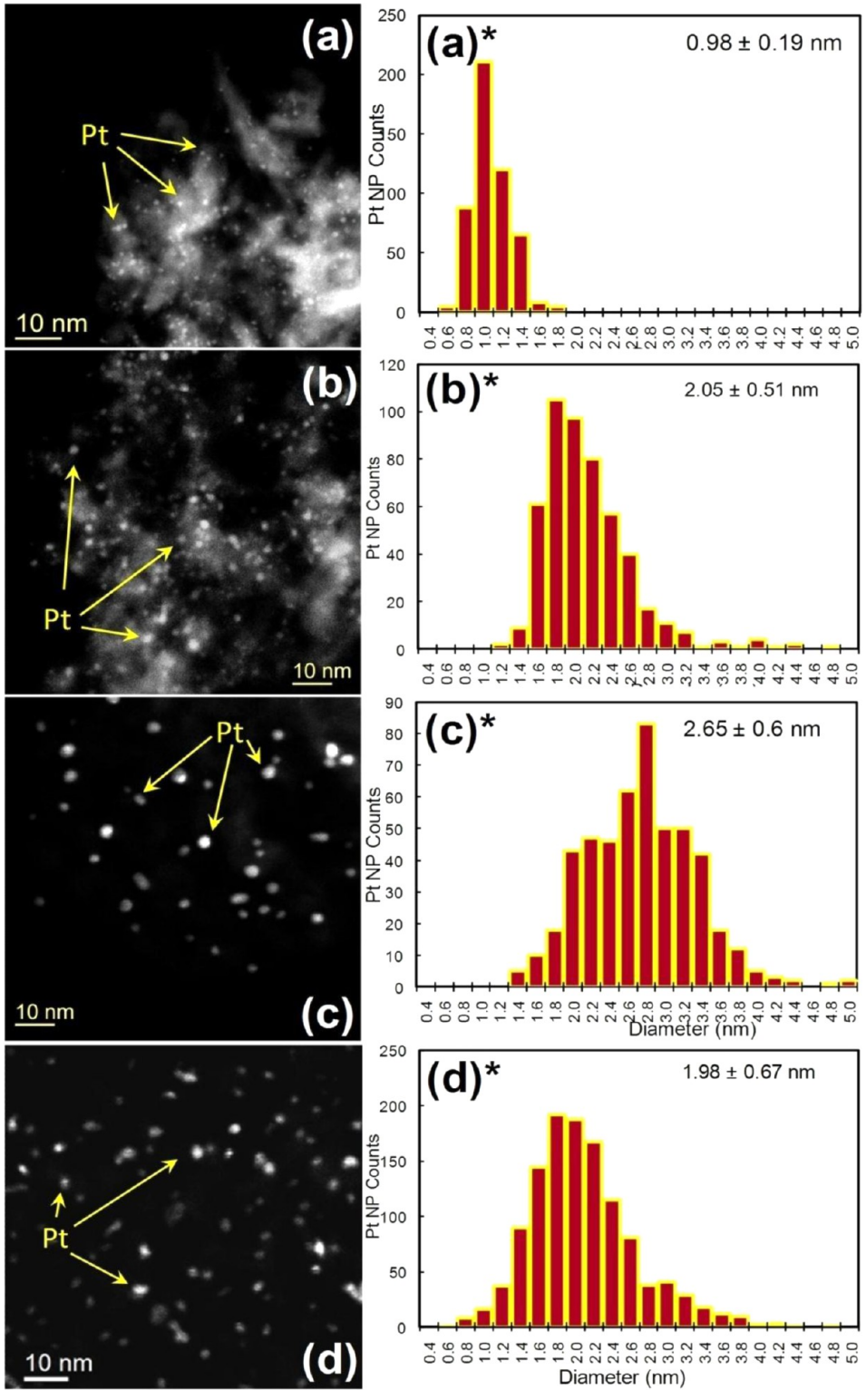

Figure 1. Representative HAADF images and corresponding NP size distributions with loading of (a) 1 wt %, (b) 3 wt %, and (c) 5 wt % Pt on γ-Al_2O_3 and (d) all Pt NPs on the C-black support.

mission electron microscopy (TEM), and scanning tunneling microscopy (STM) methodologies.[7,11−14,17,18] Of particular interest to catalysis science is the development of *in situ* characterization where the NPs' dynamics are observed under environmental conditions. Exploitation of these approaches has shown that catalyst NPs exhibit many remarkable phenomena, including significant sensitivity of their shapes, and consequently their reactivity, activity, and selectivity, to the support material, to adsorbates, and to size.[1,9−11,15,16,19−23] Despite this progress, the intuitive and convenient notion that particle structure changes monotonically with size has not been investigated.

In the nanometer scale regime, however, it has been reported that multiple structures are possible, and that a statistical

dx.doi.org/10.1021/ja405497p | J. Am. Chem. Soc. 2013, 135, 13062−13072

description is needed.[24−27] Focusing on either a few NPs (using a local method, such as TEM or STM) or their average behavior (using an ensemble method, such as EXAFS or XPS) may not accurately capture the complexity of the system. Synergistic methods provide more complete information. The combination of a local probe, such as TEM, with an ensemble averaging method, such as X-ray absorption spectroscopy (XAS), has proven to be exceptionally powerful in revealing how structural defects, strain, adsorbates, and temperature alter catalysts.[9,28−31] Herein, we report the complementary use of TEM and EXAFS with first-principles, density functional theory (DFT) calculations to focus on a fundamental material characteristic (crystalline order) and reveal a size-dependent disordering of Pt NPs that depends on support and adsorbates. Before discussing our results, details of each analysis technique are described in succession to provide clarity to and connections between the data obtained from each characterization method.

Due to their technological impact and ubiquitous study, we chose Pt NPs as the model system, studying its structural behaviors within a mesoscopic size regime of 0.6−5 nm, a range where we find the onset of the crystalline state to be statistical, not abrupt. In this report we show, using two key heterogeneous catalyst systems, Pt/C (carbon black) and Pt/γ-Al_2O_3, that a statistical description is both necessary and theoretically justified to represent their structural properties. We demonstrate the existence of a transition zone, where different structures (disordered and ordered) coexist for the same size. We also show that this transition zone is sensitive to, and tunable by, the nature of both the NP support and the presence of adsorbates. We characterize the disordered structure as "noncrystalline", to contrast it with structures that may have either long-range order or quasi-crystalline (e.g., icosahedral or decahedral) motifs.[8,24,32] This result is a surprising and nonbulk phenomenon: Disordered bulk metals exist in the molten state or as binary or ternary metallic glasses, but no example is known to date of a noncrystalline monometallic bulk.[3,33−35]

2. EXPERIMENTS AND MATERIALS

a. Synthesis of Pt Nanoparticles. Pt/γ-Al_2O_3 NPs were synthesized using the incipient wetness method to impregnate $Pt(NH_3)_4(OH)_2{\cdot}H_2O$ (Strem Chemicals, Inc.) onto the γ-Al_2O_3 support (Aldrich, surface area 220 m^2/g) with a Pt weight loading of 1% and 3%. The resulting powder was dried under vacuum, pressed into pellets and mounted into an *in situ* XAS cell. NP sizes of ∼1 or ∼2 nm were obtained by heating pellets in a stream of H_2 (4% in He) to either 573 or 687 K, respectively. The 2.9 nm Pt/γ-Al_2O_3 sample was purchased from Sigma-Aldrich and had a Pt weight loading of 5%. This sample was also pressed into a pellet and reduced at 573 K prior to XAS measurements.[23]

Pt NPs supported on carbon black were prepared in a similar manner to γ-Al_2O_3 samples. $Pt(NH_3)_4(OH)_2{\cdot}H_2O$ was impregnated onto carbon black (Cabot, Vulcan XC72, surface area 250 m^2/g) using the incipient wetness method to obtain a Pt weight loading of 1%. This precursor was then pressed into a pellet and reduced at 450 K in flowing H_2 (4% in He) to achieve 1.0 nm NPs. The Pt/C sample (10% weight loading of Pt) containing 1.8 nm NPs was commercially purchased from ETEK, Inc., pressed into a pellet and reduced at 573 K prior to XAS measurements.

b. Sample Characterization by TEM/STEM. The samples for TEM/STEM observations were prepared by crushing the pellets post EXAFS measurements to powder with anhydrous ethanol (absolute, ACS/USP grade) in an agate mortar, and then spreading one or two drops of the suspension onto a TEM Cu grid coated with an ultrathin carbon film (Ted Pella, Inc.). These samples were characterized by TEM and scanning transmission electron microscopy (STEM) techniques with a JEOL JEM 2100F TEM/STEM, which has a 200 keV field-emission gun and is equipped with a Gatan Tridiem GIF. This instrument has a point-to-point resolution of 0.23 nm, a lattice resolution of 0.1 nm [calibrated with a Au(100) single-crystal film] and an energy resolution of 1.1 eV.

The size of individual Pt NPs and size distribution histograms were measured with STEM high-angle annular dark-field (HAADF) imaging, for the three different loadings on γ-Al_2O_3 and one loadings on carbon black (Figure 1). The sizes of Pt NPs were measured based on the full width at the half-maximum value of the line intensity profile across Pt NPs on STEM HAADF images; in the case that NPs were not round, the size was based on the average of the largest and smallest measured diameters.

For Pt/γ-Al_2O_3 or Pt/C samples, a local characterization method like high-resolution TEM (HRTEM) provides direct information on the crystallinity and size of individual NPs, giving statistical information. We chose HRTEM because a parallel electron beam illuminates a wide area of the sample, in contrast to the focused beam in Z-contrast scanning TEM (STEM) often used in catalysis studies, in order to minimize the irradiation on the NP.[36,37] The determination of order versus disorder was made by acquisition of a "through-focal series" of images wherein the microscope focus was varied stepwise for effective sampling, that is, focal-series HRTEM (FS-HRTEM). Our criteria in determination of ordered/disordered NPs is based on lattice fringe observation: if lattice fringe(s) were observed in any of the images from the focal series, then the NP was classified as ordered; otherwise, it was classified as disordered. Appropriate illumination conditions were established wherein a constant electron dose did not modify the observed structures for both Pt/C and Pt/γ-Al_2O_3.

Environmental TEM (ETEM) measurements were carried out on an aberration-corrected FEI Titan 80-300 microscope. This instrument is equipped with a differentially pumped environmental cell capable of 10 Torr, and a CEOS third order postobjective image aberration corrector. High resolution TEM (HREM) imaging was carried out at 300 kV with the aberration corrector (0.1 nm information limit). The as-prepared samples were selected with an average size of 1.7 ± 0.5 nm, and ETEM samples were supported on porous nanocrystalline Si grids (SiMPore UltraSM, 5% porosity, 15 nm thick). Samples were heated to 385 °C in 1 Torr of H_2 in the ETEM column using a Gatan 652 heating holder with an Inconel furnace. Classification of the Pt NPs as "ordered" or "disordered" is similar to the method used on the JEM 2100F, where HRTEM focal series were collected in sets of 20 or 35 images.

Determination of Nanoparticle Crystallinity. In order to appropriately determine the ordered/disordered nature of Pt NPs with HRTEM imaging, we had to be concerned with several critical experimental issues, including the effect of the electron beam, the inherent visibility of the fringes, and the role of the support in suppressing the signal-to-noise in the images. In this section, a full justification of the use of this criterion is given as well as the methods by which this approach was statistically validated.

It is well-known that the incident electron beam often strongly interacts with the sample (compared to X-ray) and, especially with respect to NPs, shape, orientation and atomic structures, can be changed if the beam has a sufficient dose or dose rate.[36−48] In order to mitigate this concern, we carefully checked the beam effect for our samples: essentially, we experimentally determined a dose/dose rate which did not alter the NP configuration. This "safe illumination" was determined by choosing an electron optical configuration for the condenser optics wherein no changes were evident in either the NPs or during 15 min of imaging, where the intact nature of the ordered NPs is evident (Supporting Information Figure S1 and Movie SM1). The movie SM1 shows a segment about 5 min in length which plays 10 times faster than the real acquisition rate. The sample was Pt/γ-Al_2O_3 on a porous Si grid imaged in the TEM at high vacuum ($<2 \times 10^{-7}$ Torr) and at room temperature. We found that using a safe illumination condition is critical for the FS-HRTEM imaging to determine the order/disorder nature of Pt NPs.

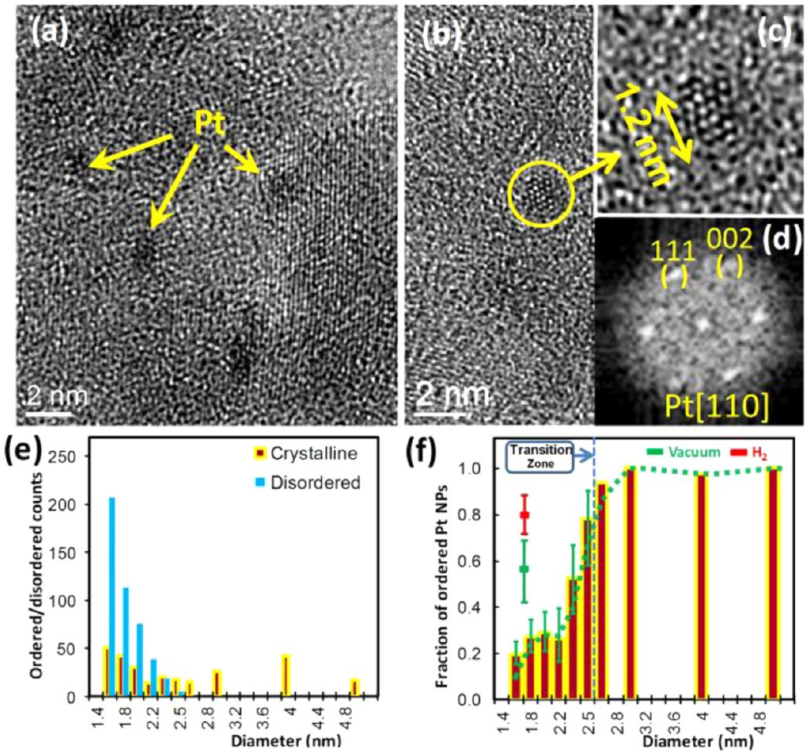

Figure 2. FS-HRTEM images and histograms of Pt NP structures on γ-Al_2O_3. (a) Disordered 1.2−1.5 nm NPs and (b) ordered 1.2 nm NP, magnified in (c) and its FFT in (d) showing fcc along [110]. (e) Histogram of ordered and disordered NPs. (f) Fraction of ordered NPs vs size, where NPs > 2.5 nm were all observed to be ordered. ETEM data in (f) were collected from many NPs: "vacuum" refers to the as-prepared samples observed in the TEM column, and "H_2" refers to ETEM data after annealing 30 min at 385 °C in 1 Torr H_2 *in situ* and then cooled to room temperature. The error bars reflect the 95% confidence interval in the data.

After establishing that it is possible to configure the electron optical configuration in such a way as to not damage the samples, the next crucial issue concerns the visibility of the lattice fringes in the NPs. This is an unresolved problem in the literature; extensive additional experimentation was conducted to establish the statistical validity of the measurements presented in Figures 2 and 3. A primary consideration is the overlap between lattice spacings in the crystals and the information limit of the instrument. Considering images obtained along all the major, low-index zone axis orientations for a face-centered cubic (fcc) lattice from ⟨001⟩ to ⟨233⟩, each of these contains one or more sets of planes with indices of {111}, {200} or {220}, and thus, for Pt in particular, this indicates interplanar spacings of 0.227 nm, 0.196 and 0.14 nm, respectively. The JEM 2100F, with a lattice resolution of 0.1 nm, is capable of resolving these lattice fringes.

However, not all NPs are oriented exactly on their zone axis (and with the extremely large number of NPs that were examined, it was not possible to systematically tilt each one to a zone axis orientation). Thus, most of the images taken of the NPs were supported on the thinnest regions of the support, and with orientations that were not along major, low-index zone axes. It is well-known for "bulk" crystalline TEM samples that the lattice fringes disappear in HRTEM images when the sample is tilted away from a low index zone axes. This is because once the sample is tilted sufficiently, the incident electron wave no longer channels effectively along the atomic columns: this results in a significant "scrambling" of the phase information present in the diffracted waves, and leads to fringe spacings that are beyond the resolution of the instrument. The situation is markedly different for crystalline NPs. As noted in prior theoretical and experimental studies,[49] NPs "are sufficiently small to possess large reciprocal-space shape functions that will be intersected by the Ewald sphere for quite large tilts away from the nearest zone axis. The electron scattering produced by these intersections will often lead to 'lattice fringes' that are not simply related to the crystal structure of the particles." As a demonstration, these authors systematically simulated HRTEM images of NPs based on a 561-atom Pd NP (a cuboctahedron), by tilting along 9 different tilts from the ⟨110⟩ orientation (at 5° increments) along 10 different tilt axes (at 10° increments), using a microscope with resolution characteristics broadly similar to that used in the present study. Each of the resulting 90 simulated images showed crystalline fringes. Similar studies (combining experiment and simulation) confirm this point.[24,50−53] Each of these papers demonstrates that there are complex interrelationships between the images and the details of the NP orientation (which can lead to significant inaccuracies in measuring lattice spacings). However, they strongly support our premise that HRTEM imaging can be an effective tool for discriminating between ordered and disordered NP structures. It is important to note that the interpretability of the observed lattice fringes with respect to the exact crystal structure is irrelevant to the assertion that the observation of fringes indicates a degree of ″crystalline″ order in the NP.

A final complexity in our work, in contrast to the studies above, is the significant role played by the support itself. Because TEM is a transmission technique, both the support and the NP contribute to the image contrast; with increasing support thickness, it is reasonable to expect that the support will dominate the image, leading to situations where lattice fringes of the NP will no longer be visible. This means the observation of crystalline fringes in very small particles becomes limited not by the native instrument resolution, but rather the signal-to-noise ratio of the experimental data. In this work, the Pt NPs of interest overlap in projection with the support, and scattering from the support can scramble the phase information in the electron waves after it has exited the NP and before it has reached the detector. This can destroy the interferences between the direct and diffracted waves that lead to the fringe contrast. Although this can be avoided, in principle, by imaging the NPs in profile, we were not able to obtain a sufficiently large number of such particles to effectively capture the statistics we needed.

dx.doi.org/10.1021/ja405497p | J. Am. Chem. Soc. 2013, 135, 13062−13072

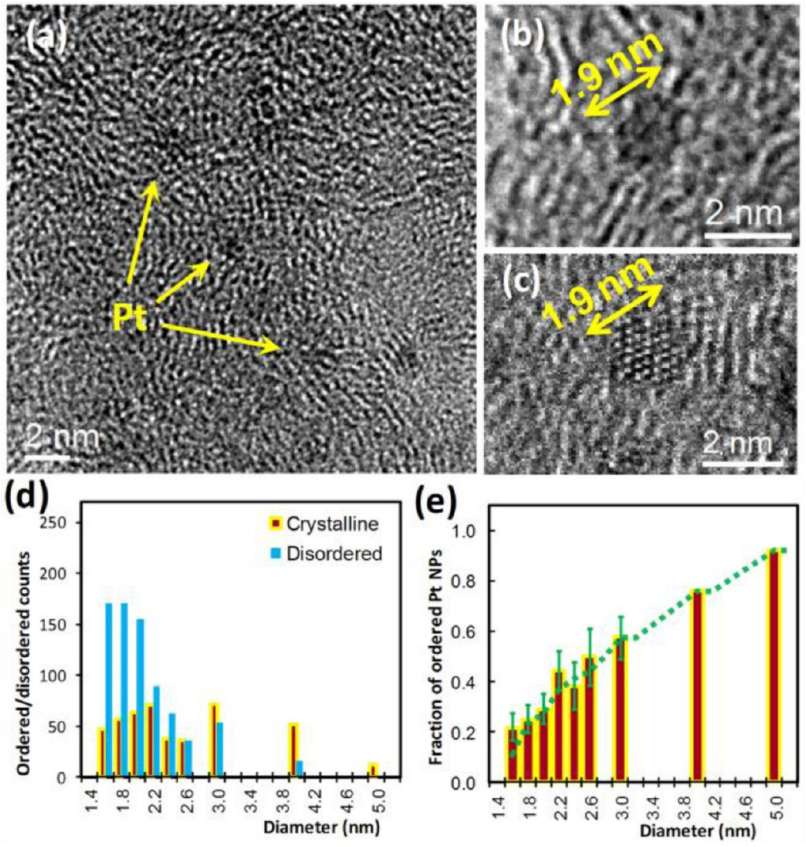

Figure 3. FS-HRTEM images and histograms of Pt NP structures on C-black. (a) Disordered NPs ≤ 1.2 nm; (b) disordered and (c) ordered 1.9 nm NPs coexist. (d) Histogram of ordered and disordered NPs. (e) Fraction of ordered NPs vs size, where NPs > 5 nm were all noted to be ordered, which is a broader transition zone than γ-Al_2O_3. The error bars reflect the 95% confidence interval in the data.

To quantify the support thickness effect on imaging, systematic examination of Au NPs on Si supports of varying thickness was performed to establish a quantitative statistical benchmark. Au NPs were selected as the model NP system because very small ordered Au NPs have been reported previously, for example, ordered 0.8 nm Au_{13} NPs on an ultrathin C-film have been imaged by HRTEM.[54] The use of Au is also intended to verify that Pt is not a special case in imaging lattice fringes for very small NPs. From this study, increasing support thickness limits both the ability to image NPs and, for smaller NPs, decreases the ordered fraction. For the support thickness of 5 nm, the EELS analysis revealed the thickness of the γ-Al_2O_3 to be 2−6 nm (Supporting Information Figure S3), significant support effects exist for particles below 1.5 nm in size, where Wilson statistical analysis gives a 95% confidence that the measured order fraction will be between 0.924 and 1.00 (Supporting Information Figure S4). In other words, for particles 1.5 nm and larger, a 95% statistical confidence exists that, *if* a particle is crystalline, lattice fringes will be visible from that particle *at least* 92.4% of the time. This forms the point where the portion of the histogram related to the NPs smaller than 1.5 nm is shown to be truncated (Figures 2 and 3). While some confidence in data obtained below 1.5 nm is reasonable, sufficient statistical confidence cannot be justifiably claimed, largely because more data from smaller Au particles is needed to obtain a 95% confidence level. These smaller particles were very rare in the as-deposited sample. However, in the spirit of full disclosure, Supporting Information Figures S5 and S6 include all of the HRTEM results.

c. Statistical Analysis. The fraction of order (1 for ordered and 0 for disordered), a dichotomous variable, follows a binomial distribution. We used 95% confidence interval as our error bars for all figures (in Figures 2f and 3e, and Supporting Information Figures S5b and S6b) based on the Wilson method. The Wilson score interval is an improvement over the normal approximation interval:[55]

$$\frac{\hat{p} + \frac{1}{2n}z_{1-\alpha/2}^{\ 2} \pm z_{1-\alpha/2}\sqrt{\frac{\hat{p}(1-\hat{p})}{n} + \frac{z_{1-\alpha/2}^{\ 2}}{4n^2}}}{1 + \frac{1}{n}z_{1-\alpha/2}^{\ 2}}$$

where n is the number of Pt (or Au) NPs (sample size for the statistics), x is the number of ordered Pt (or Au) NPs; $\hat{p} = x/n$ is the fraction of order of NPs; $z_{1-\alpha/2}$ is the $(1 - \alpha/2)$ percentile of a standard normal distribution, and α is the error percentile (e.g., for the 95% confidence level used in this paper the error (α) is 5%, $z_{1-\alpha/2}$ is 1.96).

d. XAS measurements. It should be noted that the X-ray absorption spectroscopy data described in this work had been measured previously.[23] In the present work, no additional measurements were required, although additional data analysis was performed on existing data to illuminate the order/disorder behaviors of the NPs by EXAFS, as described below.

3. THEORETICAL MODELING

DFT[56,57] with LDA[58,59] exchange-correlation functional, a plane-wave basis set and projector augmented wave method[60] as implemented in the Vienna Atomic Simulation Package (VASP)[61,62] was used. The bulk structure of γ-Al_2O_3 is best characterized as a spinel-like structure with cation defects. The bulk lattice constant of the defected spinel of γ-alumina in the fcc unit cell is 8.04 Å. To model the (100) surface, we choose a stoichiometric slab consisting of 5 layers and the atoms in the bottom two layers are fixed at the bulk positions. To accommodate Pt_{37}, a supercell of (3×3) of the tetragonal unit cell is used, which has the dimensions of 17.06 Å × 17.06 Å. With Pt_{37} we keep at least 8 Å of vacuum between neighboring slabs to avoid unphysical interaction. The slab has

dx.doi.org/10.1021/ja405497p | J. Am. Chem. Soc. 2013, 135, 13062−13072

a total of 108 O, 72 Al, and 37 Pt atoms. For carbon supports, we use a (7 × 7) graphene hexagonal supercell with dimension of 17.15 Å × 17.15 Å. For a kinetic energy cutoff of 283 eV and Γ k-point with a 0.1 eV Gaussian smearing, we found that the total energy converges within 3 meV/atom for both slabs. During ionic relaxation, the magnitudes of force on each atom were reduced below 0.02 eV/Å via conjugate-gradient. To search for lowest-energy configurations of supported NPs, ab initio molecular dynamics (MD) and simulated annealing combined with steepest-descent were used.[32]

4. RESULTS AND DISCUSSION

a. Statistical Structural Characterization of NP Crystallinity. Figure 1 is the HAADF images and corresponding size distribution histogram of the Pt NPs for the different loadings on γ-Al_2O_3 (Figure 1a–c, a*–c*) or carbon (Figure 1d, d*). The histograms represent over 3000 NPs, where the sizes of the NPs range from 0.6 to 5 nm for both supports. The identity of the support material was confirmed to be the cubic polymorph of alumina, γ-Al_2O_3, by HRTEM and electron diffraction (Supporting Information Figure S2b–e) with a lattice parameter of ~0.8 nm for $Fm\bar{3}m$. The bright-field TEM image of the support material revealed it to be composed of nanosized and polycrystalline grains (Supporting Information Figure S2a). The thicknesses of these γ-Al_2O_3 regions were determined to be 2–6 nm with ±20% error by EELS (Supporting Information Figure S3). All FS-HRTEM imaging of the Pt NPs was performed on the thin regions of the support materials.

Figures 2 and 3 present the FS-HRTEM results and statistics for Pt/γ-Al_2O_3 and Pt/C, respectively. The error bars on the fraction of disordered NPs plots (Figures 2f and 3e) reflect 95% statistical confidence based on Wilson statistics. For Pt/γ-Al_2O_3, nearly all of the Pt NPs with size > 2.6 nm revealed an fcc structure. For NPs with sizes below 2.5 nm, a transition zone exists in which a greater number of NPs are disordered, as summarized by a histogram count (Figure 2e) and fraction of crystalline NPs (Figure 2f). Similar size-dependent crystallinity is observed for Pt/C (Figure 3d and e); for example, a 1.9 nm NP could be either disordered (Figure 3b) or ordered fcc (Figure 3c). A broader transition zone is noted for Pt/C (1.5–5 nm) (Figure 3d and e) than for Pt/γ-Al_2O_3 (1.5–2.5 nm), emphasizing the critical role of the support. We note that the data presented here were truncated below 1.5 nm so that only the 95% statistically confident data is shown. In the spirit of full disclosure, we present our full data set in Supporting Information Figures S5 and S6, where NPs as small as 0.6 nm were seen, suggesting a transition zone starting a 1.1 nm for both Pt/C and Pt/γ-Al_2O_3.

Figure 4 summarizes the ETEM results. Figure 4a–c shows the size distribution, histogram, and fraction ordered from the as-prepared samples, and Figure 4d–f corresponds to the sample after exposure in 1 Torr H_2, at 385 °C for 30 min and then cooled down to room temperature in H_2 in the ETEM column. These experiments confirmed predictions that exposure to H_2 increases the crystallinity fraction at smaller sizes; that is, for 1.7 nm NPs, ~80% are ordered with H versus ~55% without H_2 (Figure 2f).

To further verify experimentally the effect of adsorbates, the ETEM results were complemented with *in situ* temperature-resolved EXAFS results to extract bond-length disorder as a function of NP size. R-space EXAFS data was obtained at room temperature on reduced NPs of the same average sizes on

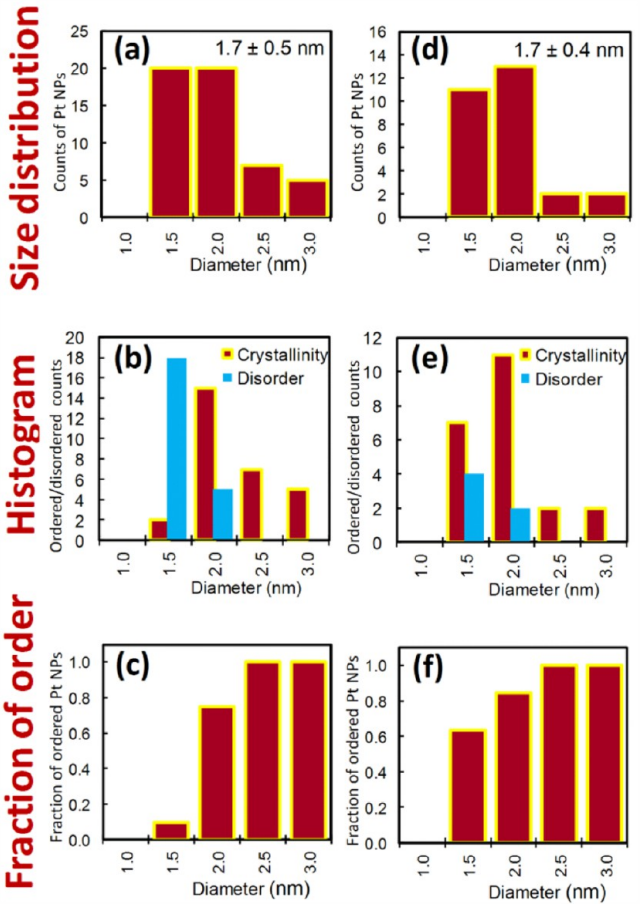

Figure 4. Histograms of the Pt NPs supported on γ-Al_2O_3 where imaging was performed on an aberration-corrected ETEM. Panels (a)–(c) correspond to the as-prepared sample, and (d)–(f) relate to the Pt NPs after exposure in 1 Torr H_2, at 385 °C for 30 min and then cooled down to room temperature in H_2. (a, d) Size distributions, (b, e) number of crystalline/disordered NPs, and (c, f) fraction of ordered NPs from the sample as prepared and after H_2 anneal, respectively.

different supports and under the flow of He(g) only or 4% H_2 in He *in situ* (Figure 5). The vertical bars on the "fcc structure" inset indicate the presence of the second and third NN Pt–Pt bonds, as well as the superposition of the 4 NN Pt–Pt bonds and collinear Pt–Pt–Pt linkages of the same lengths, which are the distinct features of the fcc structure and were noted in Pt/C under H_2.[18] The remaining NP data, including Pt/C in He and Pt/γ-Al_2O_3 in He, show a different group of features in this region, that are incompatible with an fcc structure.

The amounts of configurational disorder in Pt–Pt bonding as a function of NP size and atmosphere are shown in Figure 6. The mean-square relative displacement[18] (MSRD) of the Pt–Pt bond length was approximated as a sum of the dynamic temperature dependent disorder σ_d^2 (evaluated within an Einstein model) and the static, temperature independent disorder σ_s^2: $\sigma^2 = \sigma_d^2 + \sigma_s^2$. All the T-resolved EXAFS experiments were conducted in inert He(g) to protect the metal NPs from oxidation or in H_2(g) to study the effects of adsorption. The He exposure is similar to the high-vacuum atmosphere of the TEM. In agreement with HRTEM/ETEM results, the EXAFS results from Pt/γ-Al_2O_3 in He reveals an increasingly disordered, static (nonvibrational) distribution of Pt–Pt bond lengths with decreasing average NP sizes (Figure 6). The Pt/C EXAFS results show a similar tendency, albeit

dx.doi.org/10.1021/ja405497p | J. Am. Chem. Soc. 2013, 135, 13062–13072

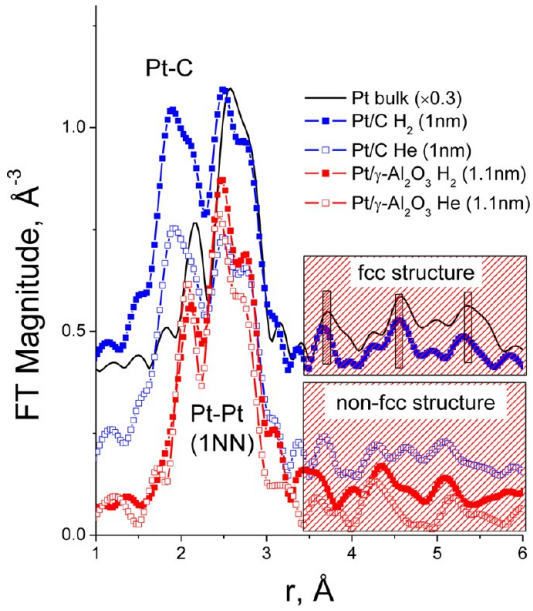

Figure 5. Fourier transform magnitudes of the R.T. EXAFS data on reduced Pt/γ-Al_2O_3 and Pt/C samples of similar average sizes: 1 and 1.1 nm, respectively. Shown also are the data for bulk Pt foil, scaled down for clarity. The Pt/C under H_2 demonstrates a local fcc-like structure, same as in Pt foil, while the rest of the samples show different types of structural order beyond the first neighbor.

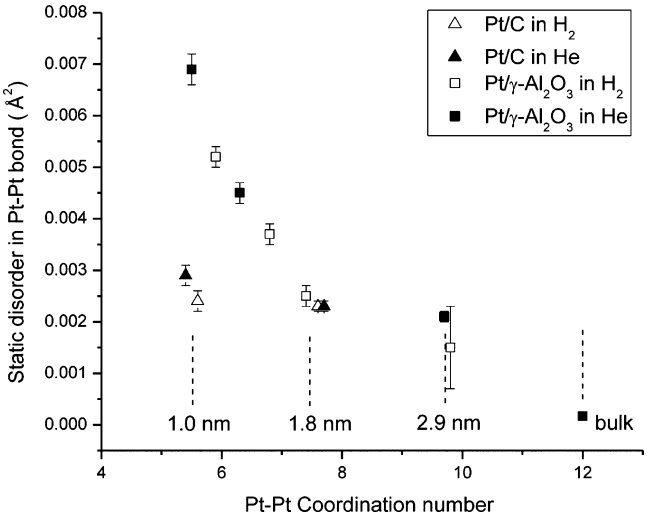

Figure 6. EXAFS analysis of static disorder for Pt/γ-Al_2O_3 and Pt/C with He and H_2.

significantly weaker. Figure 6 also shows the striking effect of H adsorbates on the crystallinity; the NPs that were disordered in He become more ordered in H_2. Thus, in situ EXAFS data agree with ETEM data regarding the enhanced NP crystallinity fraction under H_2. This same adsorbate effect is also observed in larger Pt NP on both C and γ-Al_2O_3 supports. The EXAFS results from the Pt/γ-Al_2O_3 in He atmospheres revealed an increasingly disordered distribution of Pt−Pt bond lengths with decreasing average NP sizes, in agreement with the HRTEM/ETEM data.

b. Theoretical Verification of Experimental Observations of Pt NPs Structure. The main experimental findings (from HRTEM, ETEM, and EXAFS), including (1) small particles are noncrystalline, (2) the support material stabilizes this strongly disordered phase, and (3) hydrogen adsorbates cause a crystalline fcc transition, were predicted[63] and/or corroborated by theoretical calculations of the energetically preferred NP structures. Low-energy competing structures of supported NPs are searched by ab initio MD followed by ionic relaxations. This two-step approach was used for Pt_{37}/γ-Al_2O_3(100) and Pt_{37}/C(0001)[63] with or without H adsorbates; Pt_{37} has a diameter of 1.1 nm. This theoretical modeling demonstrated that a bulk-like fcc, truncated-cuboctahedron (TC) structure can form; however, unless H adsorbates are present, the TC structure is unstable compared to a strongly disordered amorphous (Am) structure.

The calculated relative energy changes for Pt_{37} in different structural motifs and chemical environments are shown in Figure 7, along with each structure and its charge redistribution.

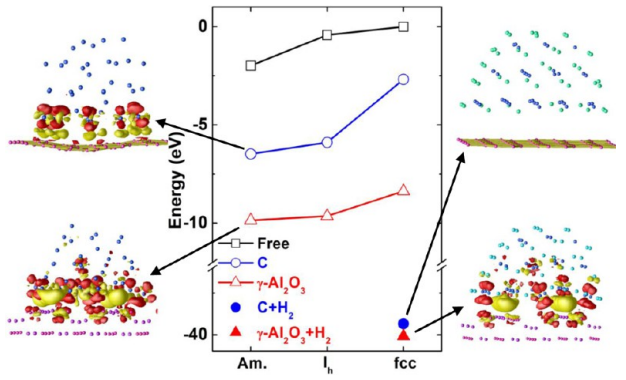

Figure 7. Relative DFT energy change for Pt_{37} in different structural motifs and chemical environments. We use relaxed freestanding TC Pt_{37}, a clean graphene layer, a clean γ-Al_2O_3 (100) slab and free H_2 as references. Freestanding NP energies (squares) and supported NP energies (circles and triangles) are relative to TC case. The H-adsorption energy is shown as filled symbols. Electron-density-differences [with ±0.04 (e/Å^3) isosurfaces and electron gain (loss) in yellow (red)] of the lowest-energy structures on C and γ-Al_2O_3 with(out) H are indicated. Spheres of dark (light) blue show the Pt (H) atoms, and magenta show support atoms.

Referenced to a freestanding TC NP and a clean support without H-passivation (or inert He), the noncrystalline structure is *always* lowest in energy both for supported and freestanding NPs for this small (1.1 nm) particle size, a result independent of the starting configuration (including I_h) and subsequent annealing. In the disordered structures, (100) facets disappear and irregular triangles formed by neighboring Pt atoms appear, but, mainly, the stability is imparted by the support. On C(0001), the disordered structure is 3.8 eV more stable than the as-adsorbed TC, while on γ-Al_2O_3 this preference is only 1.5 eV (smaller than the 2.0 eV for freestanding NP in Figure 7). This suggests that the interface interaction is more dominant in Pt/γ-Al_2O_3 than Pt/C(0001), and this is also evidenced in the charge redistribution.

Because earlier studies [ref 8 and references therein] of freestanding NPs below 10 nm indicated that crystallinity is lowered first to D_h and then I_h, a separate search was conducted, starting with a truncated I_h-derived structure by removing 18 Pt atoms in the Pt_{55} I_h cluster and putting the truncated side on the support in order to have no bias favoring fcc to I_h-derived structures. The side that is not in direct contact with support retains the unique feature of I_h, where five (111)-like facets converge to the same atomic location. The structure

dx.doi.org/10.1021/ja405497p | J. Am. Chem. Soc. 2013, 135, 13062−13072

is defined to be I_h-derived if the five converging (111)-like facets are not significantly distorted. The low-energy structures obtained in the search lose their unique I_h feature gradually and end up with a similar strongly disordered structure as those obtained with TC as the starting structure. This is confirmed experimentally by HRTEM by the rarity of NPs observed with decahedral geometry (see Supporting Information Figure S7).[24]

A qualitative argument to reconcile the different widths of the disorder-to-order transition zones (broad for C and narrow for γ-Al_2O_3) is as follows: The particle–support interaction in Pt/γ-Al_2O_3 is stronger (see Figure 7, Pt/γ-Al_2O_3 is lower in energy than Pt/C but the energy gain versus NP shape is much less, i.e., the Pt/γ-Al_2O_3 curve is more horizontal), making Pt–Pt bond-length disorder larger on γ-Al_2O_3 than on C at 1.1 nm, as seen in EXAFS (Figure 6) and theoretical Pt–Pt pair distribution functions (Figure 8). Yet, as the NP size increases, fcc appears sooner in Pt/γ-Al_2O_3 due to the smaller energy difference between disordered and fcc, leading to a narrower transition zone than on C. This may be a plausible explanation why the Pt–Pt bond length disorder is smaller for Pt/C particles compared to their Pt/γ-Al_2O_3 counterparts of the same size (Figure 6).

The adsorbate has even greater impact on structural stability. The H-passivated Pt_{37}/C is the closest to the ideal TC reference, with the least broadening in the radial distribution function (Figure 8), and is highly stabilized relative to the unpassivated NP (filled symbols, Figure 7) due to the filling of antibonding Pt *d*-states from H on the (100) facets.[63] The filling of these states removes the inherent (100)-facet shear-instability, thereby lowering the NP energy, and decreases the interaction of the NP with the C support,[63] as evident in the charge-density difference plots (Figure 7). Hence, strong order appears from disorder via H-passivation, a result also predicted for late 5*d*-based NPs. That is, from the difference in (111) and (100) surface energies, i.e., $\Delta\gamma = \gamma^{111} - \gamma^{100}$, we can compare with and without H, i.e., $\Delta\gamma_H - \Delta\gamma_0$; if this quantity is negative, an ordered NP is favored over disordered upon adsorption. For larger NPs at fixed size, the NP shape (not its TC structure) is given by a Wulff plot determined by the ratio of (100) to (111) surface energies, which may be altered by adsorption coverage. We conclude that the noncrystalline structure is preferred at very small sizes, supporting the experimental results that smaller NPs lack crystalline order, but that H can stabilize the fcc crystalline structure.

Notably, impurities are not required to produce a non-crystalline structure; it is an inherent instability and is found in other DFT studies. Hence, by Ockham's razor, one should not suspect impurities as a first cause for noncrystalline NP in environmentally controlled experiments. Indeed, for supported NPs at fixed small size, theory predicts a noncrystalline-to-crystalline transition due to H adsorption; experimentally, this is noted, for example, when at 1.7 nm much larger fractions of NPs are ordered with H (Figures 2f and Figure 4c,f). For substitutional impurities in supported NPs (e.g., binary Ir–Pt), the element with the highest vapor pressure should sit on top of the NP, unless altered by support interactions.

The experimental and theoretical results for various stable Pt NP structures are summarized in a schematic NP phase diagram (Figure 9) reflecting the effects of size and chemical environment. Within DFT, for *freestanding* NPs the amorphous phase is preferred at small sizes (at least for 1.1 nm and below for Pt). The transition to I_h and D_h happens at larger sizes[8] until fcc becomes stable (~5 nm). For *supported* small NPs

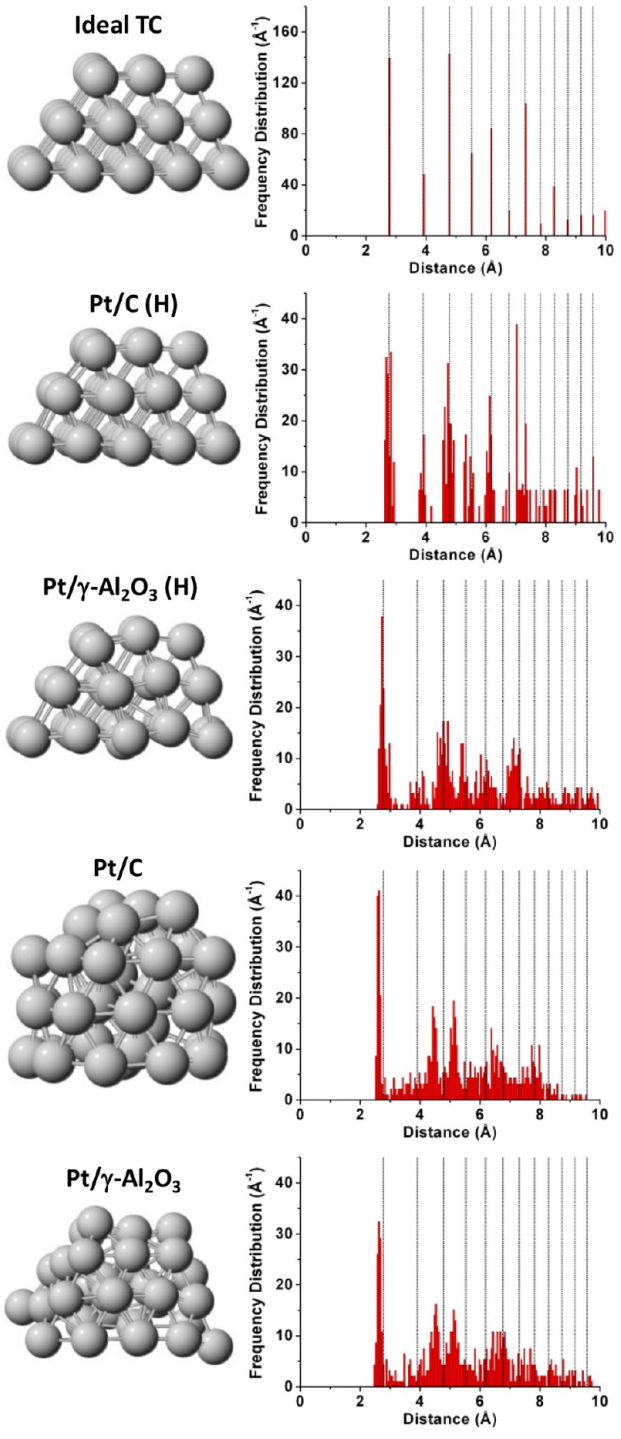

Figure 8. For the lowest-energy structures of (non)passivated, supported Pt_{37}, the calculated structure and RDF are shown. (Row 1) Unsupported ideal TC cluster as reference; supported TC cluster with (rows 2 and 3) and without (rows 4 and 5) H-passivation on C and γ-Al_2O_3, respectively; no H or support atoms are shown for clarity.

(Figure 8), a similar behavior is found but the I_h and D_h stability region is diminished due to the effects of the adsorption and support (reflected by a reduced and "fuzzy" stability region in Figure 9, where a distribution or lack of these can occur). Simulations starting with truncated fcc or I_h, structures always converge to a strongly disordered NP and show the support effect; a result born out experimentally by the rarity of decahedral NPs. When an adsorbate is added, for

dx.doi.org/10.1021/ja405497p | J. Am. Chem. Soc. 2013, 135, 13062–13072

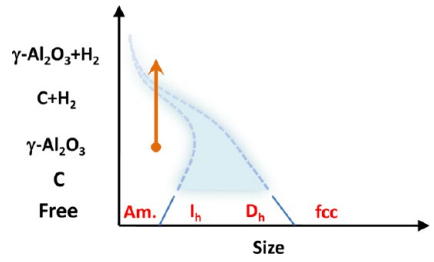

Figure 9. Schematic phase diagram of Pt NP reflecting size, support, and adsorbate. A structural transition at fixed NP size (arrow) induced by H adsorption from amorphous (disordered) to fcc (ordered) structure is exemplified. The blue shaded region indicates that the local support environment and H adsorption yield a distribution of structures, as observed in experiment (TEM, ETEM, and EXAFS) for mixtures of disordered and ordered NPs.

example, H, there can be a direct transition from noncrystalline to fcc at fixed smaller sizes (arrow in Figure 9) as predicted for Pt (and found for other late 5*d* elemental NPs) and observed in ETEM; the width of the transition zone depends on the support and adsorbates, as also found experimentally.

The stabilization of TC NP by H passivation is more generic than just Pt. The (111) and (100) surface energies with H for late 5*d* and 4*d* transition-metal elements are provided (see Table 1). In further support of these results, the details of the

Table 1. DFT-Computed H-Adsorption Energies (LDA and PBE) for Given Surface Sites[a]

	(111)			(100)		
LDA (eV)	top	hcp	fcc	top	hol	brg
Rh	−0.41	−0.84	**−0.86**	−0.47	**−0.97**	−0.89
Pd	−0.28	−0.86	**−0.91**	−0.25	**−0.92**	−0.77
Ag	0.76	−0.10	**−0.11**	0.67	**−0.06**	−0.04
Ir	**−0.65**	−0.63	−0.64	−0.83	−0.75	**−1.07**
Pt	−0.63	−0.71	**−0.76**	−0.66	−0.66	**−0.96**
Au	0.26	−0.07	**−0.08**	0.12	0.06	**−0.26**
	(111)			(100)		
PBE (eV)	top	hcp	fcc	top	hol	brg
Rh	−0.09	−0.49	**−0.50**	−0.15	**−0.57**	−0.52
Pd	0.04	−0.49	**−0.55**	0.08	**−0.51**	−0.40
Ag	1.10	0.24	**0.23**	1.01	**0.34**	0.38
Ir	**−0.37**	−0.29	−0.31	−0.53	−0.35	**−0.73**
Pt	−0.35	−0.36	**−0.41**	−0.36	−0.24	**−0.61**
Au	0.59	0.28	**0.27**	0.45	0.48	**0.11**

[a]Energies highlighted in bold indicate the most preferred sites on each surface.

H-adsorption site preferences, both for LDA and PBE exchange-correlation functionals, are shown in Table 1. Except for Ag and Pd, the (100) surface binds H stronger than (111). On (111), the fcc site is the preferred site (except for Ir). On (100), 4*d* prefers hollow sites and 5*d* the bridge sites. Also, the H-adsorption energy difference between (100) and (111) is much larger for 5*d* than 4*d*, due to the strong preference of H for the 5*d* (100) bridge sites, which can accommodate up to 2−4 monolayer coverage.

Other investigators, as enabled by the advancement of nanocharacterization tools, have also recently reported the presence of disordered NPs. Billinge et al. described a bond "softening" that may indicate enhanced disorder in Pt NPs smaller than 2 nm as well, where they used primarily synchrotron X-ray diffraction to determine the pair distribution functions.[64] Using aberration corrected STEM, Sanchez et al. noted that 5d transition metals (i.e., Ir, Pt and Au) NPs revealed a more ordered structure in comparison to their 4d counterparts (i.e., Rh, Pd and Ag), which showed a more disordered arrangement of atoms with complex systems of twinning and facets.[65] These reports support our TEM observations of disordered Pt NPs. In addition, we have performed a statistical study that demonstrates that a size-dependent distribution of order/disorder NPs exists, and that this distribution is influenced by local support environments (including possible surface defects) and H adsorbates. We have validated these observations with first-principles theoretical modeling; however, the NPs structural behavior is vastly more diverse than implied from theory using a limited sampling of NP sizes. If only a few NPs are observed (via local methods, e.g., TEM or STM) or their average behavior is studied (via ensemble methods, e.g., EXAFS or XPS), these measurements may individually not accurately capture the complexity of the whole. A statistical description is a more accurate depiction of NPs structures.

5. CONCLUSIONS

A combination of three distinct but synergistic methods (HRTEM, EXAFS, and first-principles simulations) was used to examine the nanoscale structural behaviors of supported catalysts, and to separate clearly the effects of support and chemical environments. Small Pt particles are strongly disordered, particle−support interactions control the width of the noncrystalline-to-crystalline transition zone, and H adsorbates promote the transition of TCs to crystalline fcc structures (without H, the NP size would have to be large enough to order). This result generally holds for late 5*d* elements, but not 4*d*, based on calculated adsorption site preferences. The direct observation of diverse forms of stable structures and their distribution, including noncrystalline structures, suggests that clusters over long periods sample a population of metastable states and corresponding energy barriers that significantly impacts the structural dynamics. Intriguingly, the statistical distribution of particle structures and environments indicates that an ensemble averaging of the mesoscale properties is also the appropriate description of the unusual properties of nanomaterials that are increasingly used in a wide range of technologies.

■ ASSOCIATED CONTENT

Supporting Information

Verification of the "safe illumination" condition, identification of the support material being γ-Al_2O_3 by TEM, measurement of the γ-Al_2O_3 support thickness by EELS, details of the statistical method of determining the smallest NP size where a 95% statistical confidence exists that if the NP is ordered then lattice fringes will be observed, the complete data set of the ordered/disordered Pt NPs on C and γ-Al_2O_3, and HRTEM image of a twinned NP. This material is available free of charge via the Internet at http://pubs.acs.org.

■ AUTHOR INFORMATION

Corresponding Author

judyyang@pitt.edu

Present Address

[¶]L.L.: RJ Lee Group, Inc., Monroeville, PA.

Notes

The authors declare no competing financial interest.

■ ACKNOWLEDGMENTS

This research was supported by the Office of Basic Energy Sciences (BES) of the U.S. Department of Energy (DOE) (DE-FG02-03ER15476). The ETEM was carried out at the Center for Functional Nanomaterials, Brookhaven National Laboratory (DE-AC02-98CH10886). The statistical studies of nanoparticle visibility as function of support thickness was performed at the National Center of Electron Microscopy, Lawrence Berkeley National Laboratory (DOE-BES: DE-AC02-05CH11231). The theoretical simulations were performed at Ames Laboratory which is operated by Iowa State University and supported by DOE-BES (DE-AC02-07CH11358). The HRTEM was conducted at the Nanoscale Fabrication and Characterization Facility (NFCF) at the University of Pittsburgh. L.L. kindly acknowledges RJ Lee Group, Inc. for partial support during the completion of this manuscript.

■ REFERENCES

(1) Somorjai, G. A.; Park, J. Y. *Angew. Chem., Int. Ed.* **2008**, *47*, 9212−9228.
(2) Chen, C.-C.; Herhold, A. B.; Johnson, C. S.; Alivisatos, A. P. *Science* **1997**, *276*, 398−401.
(3) Alloyeau, D.; Ricolleau, C.; Mottet, C.; Oikawa, T.; Langlois, C.; Le Bouar, Y.; Braidy, N.; Loiseau, A. *Nat. Mater.* **2009**, *8*, 940−946.
(4) Kovacs, A.; Sato, K.; Lazarov, V. K.; Galindo, P. L.; Konno, T. J.; Hirotsu, Y. *Phys. Rev. Lett.* **2009**, *103*, 115703/1−115703/4.
(5) Rao, J. *ACS Nano* **2008**, *2*, 1984−1986.
(6) Periana, R. A.; Taube, D. J.; Gamble, S.; Taube, H.; Satoh, T.; Fujii, H. *Science* **1998**, *280*, 560−564.
(7) Bell, A. T. *Science* **2003**, *299*, 1688−1691.
(8) Baletto, F.; Ferrando, R. *Rev. Mod. Phys.* **2005**, *77*, 371.
(9) Yoshida, H.; Kuwauchi, Y.; Jinschek, J. R.; Sun, K.; Tanaka, S.; Kohyama, M.; Shimada, S.; Haruta, M.; Takeda, S. *Science* **2012**, *335*, 317−319.
(10) Matthey, D.; Wang, J. G.; Wendt, S.; Matthiesen, J.; Schaub, R.; Laegsgaard, E.; Hammer, B.; Besenbacher, F. *Science* **2007**, *315*, 1692−1696.
(11) Nolte, P.; Stierle, A.; Jin-Phillipp, N. Y.; Kasper, N.; Schulli, T. U.; Dosch, H. *Science* **2008**, *321*, 1654−1658.
(12) Tao, F.; Grass, M. E.; Zhang, Y.; Butcher, D. R.; Renzas, J. R.; Liu, Z.; Chung, J. Y.; Mun, B. S.; Salmeron, M.; Somorjai, G. A. *Science* **2008**, *322*, 932−934.
(13) Somorjai, G. A.; Li, Y. *Proc. Natl. Acad. Sci. U.S.A.* **2011**, *108*, 917−924.
(14) Tao, F.; Salmeron, M. *Science* **2011**, *331*, 171−174.
(15) Newton, M. A.; Belver-Coldeira, C.; Martinez-Arias, A.; Fernandez-Garcia, M. *Nat. Mater.* **2007**, *6*, 528−532.
(16) Alayoglu, S.; Nilekar, A. U.; Mavrikakis, M.; Eichhorn, B. *Nat. Mater.* **2008**, *7*, 333−338.
(17) Hansen, P. L.; Wagner, J. B.; Helveg, S.; Rostrup-Nielsen, J. R.; Clausen, B. S.; Topsoe, H. *Science* **2002**, *295*, 2053−2055.
(18) Frenkel, A. I.; Hills, C. W.; Nuzzo, R. G. *J. Phys. Chem. B* **2001**, *105*, 12689−12703.
(19) Vajda, S.; Pellin, M. J.; Greeley, J. P.; Marshall, C. L.; Curtiss, L. A.; Ballentine, G. A.; Elam, J. W.; Catillon-Mucherie, S.; Redfern, P. C.; Mehmood, F.; Zapol, P. *Nat. Mater.* **2009**, *8*, 213−216.
(20) Lee, I.; Delbecq, F.; Morales, R.; Albiter, M. A.; Zaera, F. *Nat. Mater.* **2009**, *8*, 132−138.
(21) Zope, B. N.; Hibbitts, D. D.; Neurock, M.; Davis, R. J. *Science* **2010**, *330*, 74−78.
(22) Kwak, J. H.; Hu, J.; Mei, D.; Yi, C.-W.; Kim, D. H.; Peden, C. H. F.; Allard, L. F.; Szanyi, J. *Science* **2009**, *325*, 1670−1673.
(23) Sanchez, S. I.; Menard, L. D.; Bram, A.; Kang, J. H.; Small, M. W.; Nuzzo, R. G.; Frenkel, A. I. *J. Am. Chem. Soc.* **2009**, *131*, 7040−7054.
(24) Koga, K.; Sugawara, K. *Surf. Sci.* **2003**, *529*, 23−35.
(25) Alloyeau, D.; Ricolleau, C.; Oikawa, T.; Langlois, C.; Le Bouar, Y.; Loiseau, A. *Ultramicroscopy* **2009**, *109*, 788−796.
(26) Grothausmann, R.; Fiechter, S.; Beare, R.; Lehmann, G.; Kropf, H.; Vinod Kumar, G. S.; Manke, I.; Banhart, J. *Ultramicroscopy* **2012**, *122*, 65−75.
(27) Liu, H. H.; Schmidt, S.; Poulsen, H. F.; Godfrey, A.; Liu, Z. Q.; Sharon, J. A.; Huang, X. *Science* **2011**, *332*, 833−834.
(28) Herzing, A. A.; Kiely, C. J.; Carley, A. F.; Landon, P.; Hutchings, G. J. *Science* **2008**, *321*, 1331−1335.
(29) Farmer, J. A.; Campbell, C. T. *Science* **2010**, *329*, 933−936.
(30) Mostafa, S.; Behafarid, F.; Croy, J. R.; Ono, L. K.; Li, L.; Yang, J. C.; Frenkel, A. I.; Cuenya, B. R. *J. Am. Chem. Soc.* **2010**, *132*, 15714−15719.
(31) Small, M. W.; Sanchez, S. I.; Marinkovic, N. S.; Frenkel, A. I.; Nuzzo, R. G. *ACS Nano* **2012**, *6*, 5583−5595.
(32) Wang, L.-L.; Johnson, D. D. *Phys. Rev. B* **2007**, *75*, 235405/1−10.
(33) Siegrist, T.; Jost, P.; Volker, H.; Woda, M.; Merkelbach, P.; Schlockermann, C.; Wuttig, M. *Nat. Mater.* **2011**, *10*, 202−208.
(34) Doye, J. P. K.; Wales, D. J. *Science* **1996**, *271*, 484−487.
(35) Byrne, C. J.; Eldrup, M. *Science* **2008**, *321*, 502−503.
(36) Egerton, R. F.; Wang, F.; Crozier, P. A. *Microsc. Microanal.* **2006**, *12*, 65−71.
(37) Batson, P. E. *Microsc. Microanal.* **2008**, *14*, 89−97.
(38) Bovin, J. O.; Wallenberg, R.; Smith, D. J. *Nature* **1985**, *317*, 47−9.
(39) Smith, D. J.; Petford-Long, A. K.; Wallenberg, L. R.; Bovin, J. O. *Science* **1986**, *233*, 872−5.
(40) Iijima, S. *J. Electron Microsc.* **1985**, *34*, 249−265.
(41) Iijima, S.; Ichihashi, T. *Phys. Rev. Lett.* **1986**, *56*, 616−19.
(42) Egerton, R. F.; Li, P.; Malac, M. *Micron* **2004**, *35*, 399−409.
(43) Howie, A.; Rocca, F. J.; Valdrè, U. *Philos. Mag. B* **1985**, *52*, 751−757.
(44) Varlot, K.; Martin, J. M.; Quet, C.; Kihn, Y. *Ultramicroscopy* **1997**, *68*, 123−133.
(45) Libera, M. R.; Egerton, R. F. *Polym. Rev.* **2010**, *50*, 321−339.
(46) Marks, L. D. *Rep. Prog. Phys.* **1994**, *57*, 603−49.
(47) Doraiswamy, N.; Marks, L. D. *Surf. Sci.* **1996**, *348*, L67−L69.
(48) Gryaznov, V. G.; Kaprelov, A. M.; Kaprelov, A. M.; Belov, A. Y. *Philos. Mag. Lett.* **1991**, *63*, 275−279.
(49) Malm, J. O.; O'Keefe, M. A. *Ultramicroscopy* **1997**, *68*, 13−23.
(50) Ascencio, J. A.; Gutiérrez-Wing, C.; Espinosa, M. E.; Marín, M.; Tehuacanero, S.; Zorrilla, C.; José-Yacamán, M. *Surf. Sci.* **1998**, *396*, 349−368.
(51) Flores, A. B.; Robles, L. A.; Arias, M. O.; Ascencio, J. A. *Micron* **2003**, *34*, 109−118.
(52) Fraundorf, P.; Qin, W.; Moeck, P.; Mandell, E. *J. Appl. Phys.* **2005**, *98*, 114308/1−114308.
(53) Zhang, J.; Tang, Y.; Lee, K.; Ouyang, M. *Science* **2010**, *327*, 1634−1638.
(54) Menard, L. D.; Xu, H.; Gao, S.-P.; Twesten, R. D.; Harper, A. S.; Song, Y.; Wang, G.; Douglas, A. D.; Yang, J. C.; Frenkel, A. I.; Murray, R. W.; Nuzzo, R. G. *J. Phys. Chem. B* **2006**, *110*, 14564−14573.
(55) Brown, L. D.; Cai, T. T.; DasGupta, A. *Stat. Sci.* **2001**, *16*, 101−117.
(56) Hohenberg, P.; Kohn, W. *Phys. Rev.* **1964**, *136*, B864−B871.
(57) Kohn, W.; Sham, L. J. *Phys. Rev.* **1965**, *140*, A1133−A1138.
(58) Ceperley, D. M.; Alder, B. J. *Phys. Rev. Lett.* **1980**, *45*, 566−569.
(59) Perdew, J. P.; Zunger, A. *Phys. Rev. B* **1981**, *23*, 5048−5079.
(60) Blöchl, P. E. *Phys. Rev. B* **1994**, *50*, 17953−17979.
(61) Kresse, G.; Furthmüller, J. *Comput. Mater. Sci.* **1996**, *6*, 15−50.
(62) Kresse, G.; Furthmüller, J. *Phys. Rev. B* **1996**, *54*, 11169−11186.
(63) Wang, L.-L.; Johnson, D. D. *J. Am. Chem. Soc.* **2007**, *129*, 3658−3664.

(64) Shi, C.; Redmond, E. L.; Mazaheripour, A.; Juhas, P.; Fuller, T. F.; Billinge, S. J. L. *J. Phys. Chem. C* **2013**, *117*, 7226−7230.
(65) Sanchez, S. I.; Small, M. W.; Bozin, E. S.; Wen, J.-G.; Zuo, J.-M.; Nuzzo, R. G. *ACS Nano* **2012**, *7*, 1542−1557.